RSC Advances

PAPER

View Article Online
View Journal | View Issue

Cite this: *RSC Adv.*, 2025, **15**, 34406

Preparation and electromagnetic-wave-absorption properties of nitrogen-doped carbon microsphere/iron cobalt alloy composite

Lifen He, *[a] Ru Wang,[b] MingYue Deng,[a] Min Jin,[a] Yujia Wu[a] and Xiaoyun Long [c]

The fast progress in wireless communication technology has significantly intensified electromagnetic interference, underscoring the urgent need for developing high-efficiency, low-cost microwave-absorbing materials (MAMs). The current work synthesizes polydopamine microspheres, which can adsorb Co^{2+} and Fe^{3+}, followed by the preparation of a nitrogen-doped carbon microsphere/iron cobalt alloy composite microwave absorbing material (NCS/FeCo) *via in situ* reduction through high-temperature calcination. Additionally, the surface morphology, surface element composition, hysteresis loop, and electromagnetic parameters were investigated, and the reflection loss (RL) was obtained to explore the absorbing mechanism. The results demonstrated that at a 2.5 mm NCS/FeCo thickness, the maximum RL at 13.4 GHz was −55.3 dB, with the corresponding effective absorption bandwidth (EAB) of 11.28 GHz (6.72–18 GHz). Furthermore, the material exhibits excellent microwave-absorbing properties, providing valuable insights to develop efficient microwave-absorbing materials.

Received 28th July 2025
Accepted 8th September 2025

DOI: 10.1039/d5ra05446j

rsc.li/rsc-advances

1 Introduction

The advancement of science and technology has resulted in the extensive usage of electronic equipment and communication technology, leading to increasingly serious electromagnetic radiation pollution in the 2–18 GHz band.[1] In addition to damaging electronic equipment, electromagnetic interference also harms human health and causes diseases such as immune system damage.[2] The two main approaches to address the issue are: electromagnetic shielding and electromagnetic wave absorption (EWA). The former protects by reflecting electromagnetic waves.[3] However, it poses a risk of secondary pollution. The latter converts electromagnetic waves into heat through the energy conversion mechanism, making it a more promising means of pollution control.[4]

In particular, electromagnetic wave-absorbing materials (WAMs) are crucial for stealth technology in the military area. The advancement of radar detection technology has promoted stealth technology to become the core aspect of modern war to reduce the target radar cross-section (RCS).[5] Stealth technology includes shape stealth (for instance, the AGM-129 missile weakens the reflection source through structural design, although this approach is costly and affects operational performance), impedance loading, and material stealth. Among these, material stealth is achieved by coating radar-absorbing materials. A typical example is the U.S. F-117A fighter, which uses multiple types of radar-absorbing coatings to significantly reduce detectability. This method offers the advantages of universality and low cost, making it suitable for all kinds of weapons and equipment. Hence, it has become the main focus in the development of military stealth technology. Electromagnetic wave-absorbing materials hold significant strategic value in the fields of civil environmental protection and national defense science and technology.

It is challenging for a single loss mechanism to simultaneously fulfill the needs of "thin, light, wide, and strong". Notably, an excessively high dielectric constant or permeability leads to impedance matching (IM) imbalance, which does not effectively contribute to electromagnetic loss. As is well-known, an electromagnetic wave comprises two dependent components: magnetic and electric fields. The absorption of electromagnetic wave energy is more favorable if the electromagnetic wave-absorbing material simultaneously has dielectric and magnetic losses. Therefore, it is crucial to design composite electromagnetic wave-absorbing materials involving dielectric and magnetic losses by optimizing a combination of low-density dielectric and strong absorption magnetic loss materials.[6–8]

Currently, numerous researchers at home and abroad are primarily focused on developing composite electromagnetic WAMs. Li *et al.*[9] established a carbon-coated FeCo alloy modified on porous RGO nanosheets (FeCo@C/HRGO) using the liquid-phase alleviation method, hydrothermal approach, and high-temperature calcination method. The maximum reflection

[a]*College of Safety Engineering and Emergency Management, Nantong Institute of Technology, NanTong 226000, China. E-mail: 20239373@ntit.edu.cn*
[b]*Pei County Secondary Specialized School of Jiangsu Province, XuZhou 221661, China*
[c]*National & Local Joint Engineering Research Center of Technical Fiber Composites for Safety and Protection, Nantong University, NanTong 226000, China*

loss (RL) is −76.6 dB at 16.64 GHz at a 1.7 mm thickness, while the effective absorption bandwidth (EAB) is 14.32 GHz in the thickness interval of 1.7–5.0 mm. Notably, the EWA efficiency is significantly improved compared to the single FeCo alloy. Li *et al.*[10] combined the argon liquid-phase reduction method with the hydrothermal method to prepare FeCo@SiO_2@RGO composite, which exhibits excellent dielectric and magnetic loss features. The maximum RL is −52.9 dB at 9.12 GHz at a 3.0 mm thickness, while the EAB is 5.36 GHz (8.8–14.16 GHz) at 2.5 mm. It is an excellent electromagnetic WAM. Bao *et al.*[11] successfully synthesized Fe_3O_4/FeCo/C composite microspheres including a magnetic three-shell hollow structure using a three-step method. The maximum reflection loss is −37.4 dB, with an EAB up to 5.9 GHz. The FeCo alloy enhances the material's microwave absorption mechanism at various frequencies, while C protects Fe_3O_4 and FeCo from oxidation. Wen *et al.*[12] prepared a cobalt metal organic structure@mesoporous polydopamine composite including a core–shell framework using the bottom-up assembly method (Co-MOF@MPDA). Following calcination, a Co@S-doped carbon core and mesoporous N-doped carbon shell were obtained (Co@SC@MNC). It should be noted that the doping of N increases the polarization loss of the dipole. The dielectric loss and magnetic loss can be adjusted by controlling the calcination temperature, thereby improving the impedance matching while enhancing the efficiency of electromagnetic wave absorption. The maximum RL is −72.3 dB, including a 6.0 GHz effective absorption bandwidth. Xiong *et al.*[13] synthesized a tomato-like layered porous composite (FeCo/C@WC) through a light anisotropic wood carbon aerogel (WC) as a constructional additive and MOF-derived graphite carbon-coated FeCo alloy (FeCo/C) as a microwave-absorbing modifier. The macroporous wood shell and mesoporous carbon nanocage provide a layered dielectric coupling network for the mixture, while the evenly scattered FeCo nanoparticles promote the magnetic loss, achieving better IM. The maximum RL of FeCo/C@WC is −47.6 dB, including a 8.9 GHz effective absorption bandwidth.

Magnetic metal alloys are ferromagnetic alloy materials, mainly composed of Fe, Co, and Ni. The band hybridization between constituent elements can have novel effects on electromagnetic properties.[11–14] Therefore, the preparation of carbon material/magnetic metal alloy electromagnetic wave-absorbing composites provides new opportunities for exploring more efficient electromagnetic wave-absorbing materials.

The current work synthesizes polydopamine microspheres using dopamine monomer as the raw material through a self-polymerization reaction. Due to the high surface activity of dopamine, Co^{2+} and Fe^{3+} were adsorbed. Subsequently, the nitrogen-doped carbon microspheres/FeCo alloy composite microwave absorbing material (NCS/FeCo) was prepared by *in situ* reduction through the high-temperature calcination method. Compared with previously reported technologies,the proposed synthesis method is more convenient, stable, and offers enhanced structural controllability, which contributes to the superior microwave absorption performance of the prepared composite. In the preparation process, the introduced polydopamine (PDA) can not only act as a nitrogen source—avoiding the problems of uneven nitrogen distribution and cumbersome preparation steps caused by the additional addition of urea or melamine—but also, by virtue of its dual-sided modification property, enable the uniform dispersion and firm loading of FeCo. This solves the issues typically encountered when FeCo is composited with matrix materials *via* traditional methods (*e.g.*, physical mixing, impregnation–calcination), such as particle agglomeration and weak bonding force with the carbon matrix. Additionally, the morphology distribution, chemical composition, disorder degree, and magnetic and electromagnetic parameters of the NCS/FeCo composite were characterized and analyzed. Moreover, the RL was computed to explore the microwave-absorbing mechanism, providing data support and insights into the construction of efficient microwave-absorbing materials (MAMs).

2 Experiments

2.1 Chemicals

All chemicals were of analytical grade and used without further purification. Dopamine hydrochloride (DA) was obtained from Shanghai Debai Co., Ltd. Ammonium hydroxide ($NH_3 \cdot H_2O$), absolute ethanol, and iron(III) chloride hexahydrate ($FeCl_3 \cdot 6H_2O$), cobalt chloride ($CoCl_2 \cdot 6H_2O$) were bought from Xilong Science Co., Ltd and Sinopharm Reagent Co., Ltd, respectively. Methanol was acquired from Shanghai Revitalization Co., Ltd.

2.2 Synthesis of the NCS/FeCo composite

Fig. 1 illustrates the preparation process of NCS/FeCo.

For the experiment, 30 ml of CH_3OH and 1 ml of $NH_3 \cdot H_2O$ were incorporated into 120 ml of deionized water while stirring with a magnetic force for half an hour. After adding 0.5 g of dopamine hydrochloride (DA), the mixture was stirred continuously for 30 hours, frequently washed using deionized water and anhydrous ethanol while drying in the furnace at 60 °C for 12 h to finally acquire the PDA powder. The resulting PDA powder was added to 100 mL of deionized water, and the powder was uniformly scattered using ultrasonic treatment for 10 min. 0.357 g of $CoCl_2 \cdot 6H_2O$ was then added and stirred for 5 hours. Subsequently, 0.2705 g of $FeCl_3 \cdot 6H_2O$ was added and continuously stirred for 15 hours, centrifuged and washed with deionized water while drying in the furnace at 60 °C for 12 hours. In the end, the dried sample was calcined using a muffle oven at 750 °C under a nitrogen atmosphere for 2 hours, with a 5 °C min^{-1} heating rate. The final sample was named NCS/FeCo.

2.3 Characterization and measurements

2.3.1 SEM test of NCS/FeCo. A Gemini 300 field emission scanning electron microscope (SEM) constructed by the Carl Zeiss company in Germany was employed to characterize the NCS/FeCo's surface morphology. The test voltage was 5 kV, and the sample surface was sprayed with gold.

2.3.2 TEM test of NCS/FeCo. A Jeol-2100 field emission transmission electron microscope (TEM) manufactured by

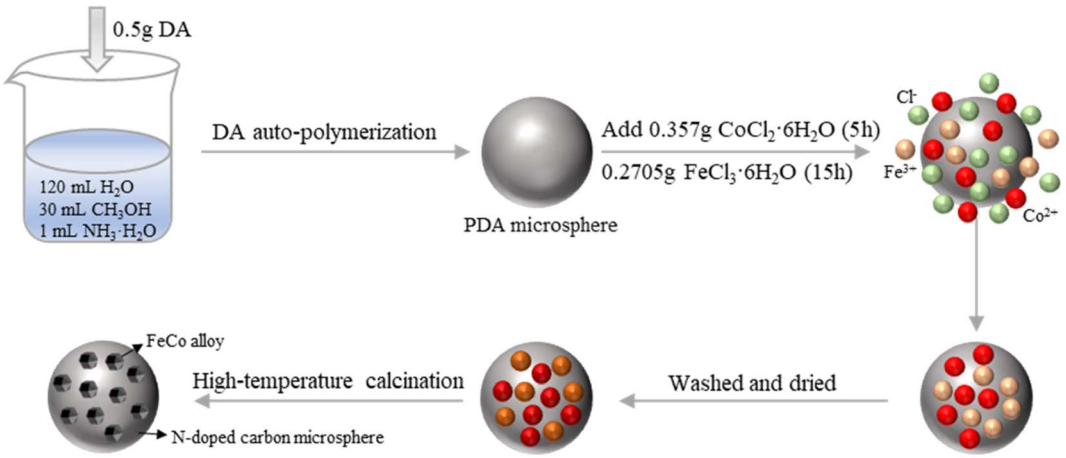

Fig. 1 Flowchart of NCS/FeCo preparation.

Japan Electronics Co., Ltd was utilized to describe the internal structure of NCS/FeCo.

2.3.3 XRD test of NCS/FeCo. The NCS/FeCo's phase framework was characterized using a RIGAKU D/max-2500pc X-ray diffractometer (XRD) manufactured by Japan RIKEN Co., Ltd. The scanning interval and velocity were 10–80° and 5° min^{-1}, respectively. The X-ray source is a Cu target including a 1.5406 Å wavelength. The test was conducted at a 40 kV voltage and a 40 mA test current.

2.3.4 XPS test of NCS/FeCo. The chemical composition of NCS/FeCo was characterized through an ESCALAB-250xi X-ray photoelectron spectrometer (XPS) produced by Thermo Fisher Scientific. The X-ray source is a monochromatic Al target, with a wavelength of 0.8339 nm and a test voltage of 15 kV.

2.3.5 Raman test of NCS/FeCo. The degree of disorder in NCS/FeCo was characterized using a Thermo Scientific DXR2 Raman spectrometer manufactured by Thermo Fisher Scientific, with a wavelength of 532 nm.

2.3.6 VSM test of NCS/FeCo. The saturation magnetization, coercivity, and other magnetic parameters of NCS/FeCo were characterized using the MPMS3 magnetic measurement system. The measurement temperature was 300 K with a measurement range of −30000–30000 Oe.

2.3.7 Electromagnetic parameter test of NCS/FeCo. The electromagnetic parameters (complex permittivity and permeability) of NCS/FeCo in a 2–18 GHz frequency interval were described using a coaxial approach through a vector network analyzer (VNA) (Ceyear AV3672C). The NCS/FeCo powder and paraffin were evenly combined at a 1 : 4 weight ratio and subsequently pressed into the mold to make a coaxial ring with an outer and inner diameters of 7 mm and 3.04 mm, respectively.

3 Results and discussion

3.1 Examination of surface morphology

As depicted in Fig. 2, the microstructure of NCS/FeCo was characterized using SEM and TEM approaches. Fig. 2(a) illustrates the SEM diagram of NCS/FeCo, and Fig. 2(b) and (c) depict the TEM diagrams of NCS/FeCo. Notably, NCS/FeCo exhibits a regular and round morphology with clear particles on the surface, which is likely the alloy formed due to FeCo agglomeration. Fig. 2(d) presents the NCS/FeCo's high-resolution TEM (HRTEM) image, revealing the lattice stripes having a distance of 0.2 nm between planes, compatible with the (110) plane of FeCo alloy.[15] This indicates the excellent reduction of Fe^{3+} and Co^{2+} to FeCo alloy under high-temperature conditions.

The distribution of main elements on the surface of NCS/FeCo was further studied through energy-dispersive X-ray spectroscopy (EDS). The EDS diagram displayed in Fig. 3 confirms that the C, O, and N elements are evenly distributed on the NCS/FeCo surface. Meanwhile, in addition to the larger FeCo particles presented in Fig. 2(b) and (c), Fe and Co elements are evenly distributed across the surface of carbon microspheres. This results in the formation of more carbon/magnetic heterogeneous interfaces, thereby improving the material's microwave absorption efficiency.

3.2 Analysis of surface phase composition

Fig. 4 shows the phase structure of NCS/FeCo characterized by XRD. Notably, a wide diffraction peak is observed in the range of 20–30°, indicating that the carbon in NCS/FeCo is mainly amorphous. Moreover, the characteristic peaks at 44.7°, 65.2°, and 82.3° are related to FeCo alloy's (110), (200), and (211) crystal planes,[16] suggesting that the composite predominantly contains FeCo alloy. Additionally, a relatively weak diffraction peak is noted at 35.7°, representing the (311) crystal plane of $CoFe_2O_4$,[17] which may indicate the incomplete reduction of $CoFe_2O_4$ during high-temperature calcination.

In the preparation stage prior to high-temperature calcination, polydopamine (PDA) can form stable chelating structures with Fe^{3+}/Co^{2+} *via* the catechol hydroxyl groups (–OH) and amino groups ($–NH_2$) in its molecular structure. Specifically, the amino groups further bind to metal ions through lone pairs of electrons, collectively constructing "Fe^{3+}/Co^{2+}-PDA" chelates. This pre-chelating effect modifies the electron cloud distribution of Fe/Co ions: the electron density of metal ions is

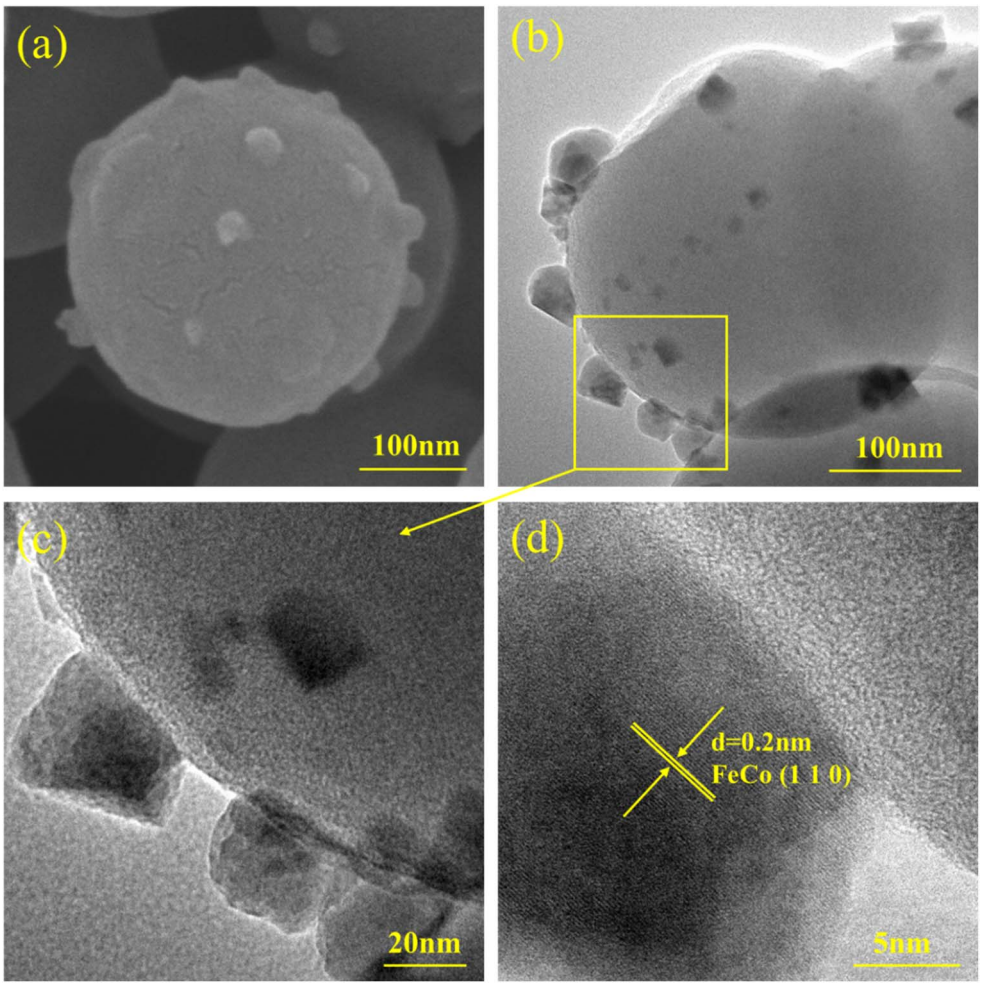

Fig. 2 Topography of NCS/FeCo obtained with various techniques: (a) SEM; (b and c) TEM; (d) HRTEM.

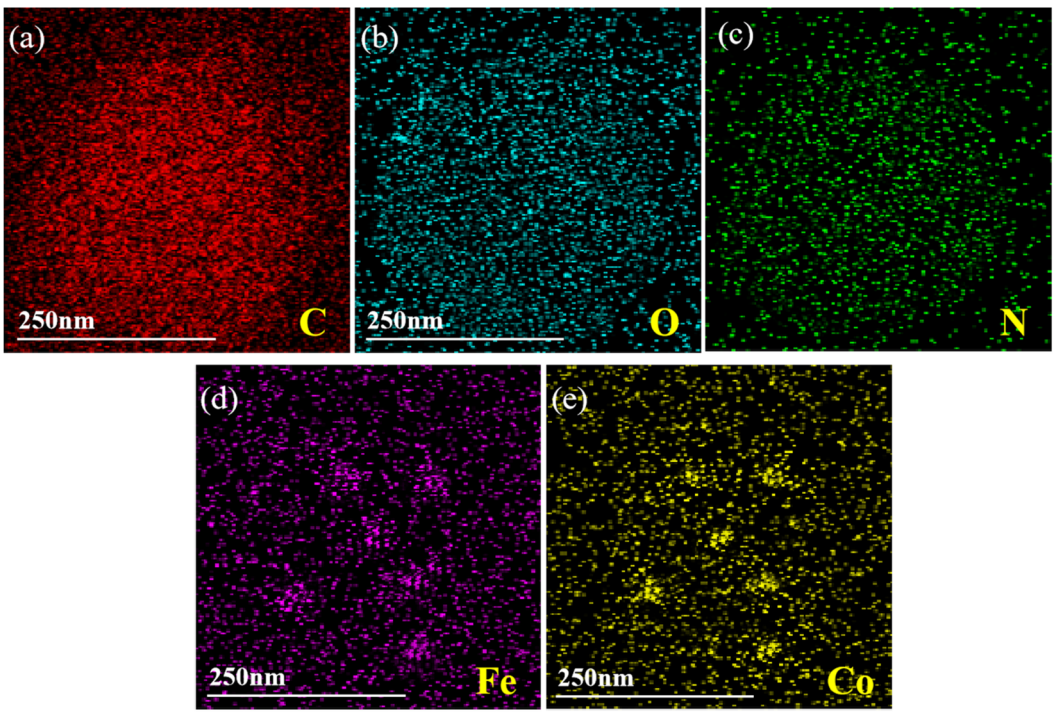

Fig. 3 EDS map of NCS/FeCo: (a) C; (b) O; (c) N; (d) Fe, and (e) Co.

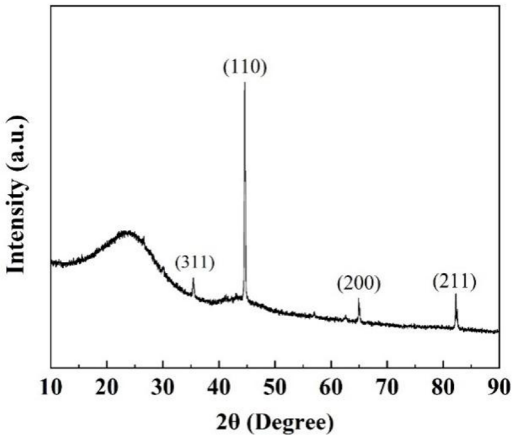

Fig. 4 XRD pattern of NCS/FeCo.

significantly increased due to the coordination interaction, making them more prone to accepting electrons during subsequent calcination and thus creating favorable conditions for the reduction reaction.

During the high-temperature calcination process under a nitrogen atmosphere, PDA undergoes carbonization and is converted into a nitrogen-doped carbon matrix (NCS)—this process is not merely a simple structural transformation, but is also accompanied by the *in situ* release of electrons: the C–H bonds and C–C bonds in PDA molecules break at high temperatures, generating a large number of reductive active carbon intermediates (*e.g.*, carbon free radicals, low-valent carbon species). These active carbon intermediates can act as electron donors, directly transferring electrons to the chelated Fe^{3+}/Co^{2+} and efficiently promoting the reduction of Fe^{3+}/Co^{2+} to FeCo alloy.

3.3 Surface element analysis

Fig. 5 shows the chemical composition of NCS/FeCo characterized by the XPS test.

Fig. 5(a) describes the NCS/FeCo's full-width scanning spectrum, which includes the characteristic maximums of C 1s, N 1s, O 1s, Fe 2p, and Co 2p.

Fig. 5(b) presents the high-resolution energy spectrum of C 1s of NCS/FeCo. The C 1s is fitted to four peaks including binding energies of 283.38, 284.28, 285.43, and 287.93 eV, corresponding to C–C, C–N, C–O, and C=O bonds.[18]

Fig. 5(c) displays the high-resolution energy spectrum of N 1s of NCS/FeCo. Here, the N 1s is fitted to three peaks with binding energies of 397.08, 399.48, and 402.43 eV, corresponding to graphite-N, pyrrole-N, and pyridine-N, respectively.[18] The presence of N improves electromagnetic wave absorption performance. Pyridine-N (402.43 eV) and pyrrole-N (399.48 eV) can form stable N–Fe/Co coordination bonds with the unsaturated metal sites on the surface of FeCo particles *via* the lone pairs of electrons in their molecular structures. This directional coordination effect enables FeCo particles to be firmly anchored on the surface of PDA-derived carbon microspheres, preventing particle agglomeration during high-temperature calcination and thereby constructing a tight carbon/magnetic heterogeneous interface.

Meanwhile, the difference in interfacial electronegativity between N element and FeCo particles drives the redistribution of charges in the interface region, forming a large number of "interfacial dipoles". Under the action of an alternating electromagnetic field, this interfacial chemical property can significantly enhance the interfacial polarization effect between the carbon matrix and FeCo particles, thereby improving the material's electromagnetic wave dissipation capacity and enhancing its microwave absorbing performance.

Fig. 5(d) presents the high-resolution energy spectrum of O 1s of NCS/FeCo. The O 1s was fitted to five peaks including binding energies of 528.93, 529.88, 531.03, 532.38, and 534.92 eV, respectively, corresponding to metal–O, C–O=N, C=O, C–OH, and C–O–C bonds.[19,20] The oxygen-including functional group serves as the polarization center, improving the material's dipole polarization and polarization relaxation, thereby attenuating the incident electromagnetic wave. The metal–O bond formation is likely attributed to the chelation of oxygen-including functional groups in PDA including metal ions to construct ligands. Notably, Fe^{3+} and Co^{2+} are reduced to FeCo alloy following high-temperature heat treatment while growing on the surface of carbon microspheres.

Fig. 5(e) describes the high-resolution energy spectrum of Fe 2p of NCS/FeCo. The Fe 2p spectrum is fitted to four main peaks and two satellite peaks. The main peak at 707.75 eV represents Fe metal, indicating the presence of FeCo alloy. Moreover, the two main peaks at 709.34 and 711.12 eV represent octahedral Fe^{2+} and tetrahedral Fe^{3+}, respectively. These three main peaks correspond to the Fe $2p_{3/2}$'s spin–orbit peak,[21] with the corresponding satellite peak at 716.18 eV. The primary peak at 723.69 eV is related to the spin–orbit peak of Fe $2p_{1/2}$,[22] with the corresponding satellite peak at 731.85 eV.

Fig. 5(f) describes the high-resolution energy spectrum of Co 2p of NCS/FeCo. Here, three main peaks and two satellite peaks are fitted by Co 2p. The main peak at 777.98 eV represents Co metal, indicating the presence of FeCo alloy; the main peak at 779.81 eV represents Co^{2+}, both of which correspond to the Co $2p_{3/2}$'s spin–orbit peak,[23] with the corresponding satellite peak at 784.71 eV. The primary peak at 795.09 eV depends on the spin–orbit peak of Co $2p_{1/2}$,[24] with the corresponding satellite peak at 801.91 eV.

3.4 Raman analysis

Raman spectroscopy is often used to analyze the carbon atoms' state and the graphitization degree in carbon materials. The unique spectral characteristics of carbon materials in Raman spectroscopy are the D-band and G-band, which are crucial means for researchers to study carbon-based materials. Generally, the D-band appears around 1365 cm^{-1}, and its appearance reveals the existence of deficiencies in carbon materials, such as the absence of atoms or the shift of atomic positions. The G-band, appearing near 1595 cm^{-1}, is attributed to the sp^2 hybrid carbon atoms in carbon materials and indicates the plane vibration of the lattice structure of graphite.

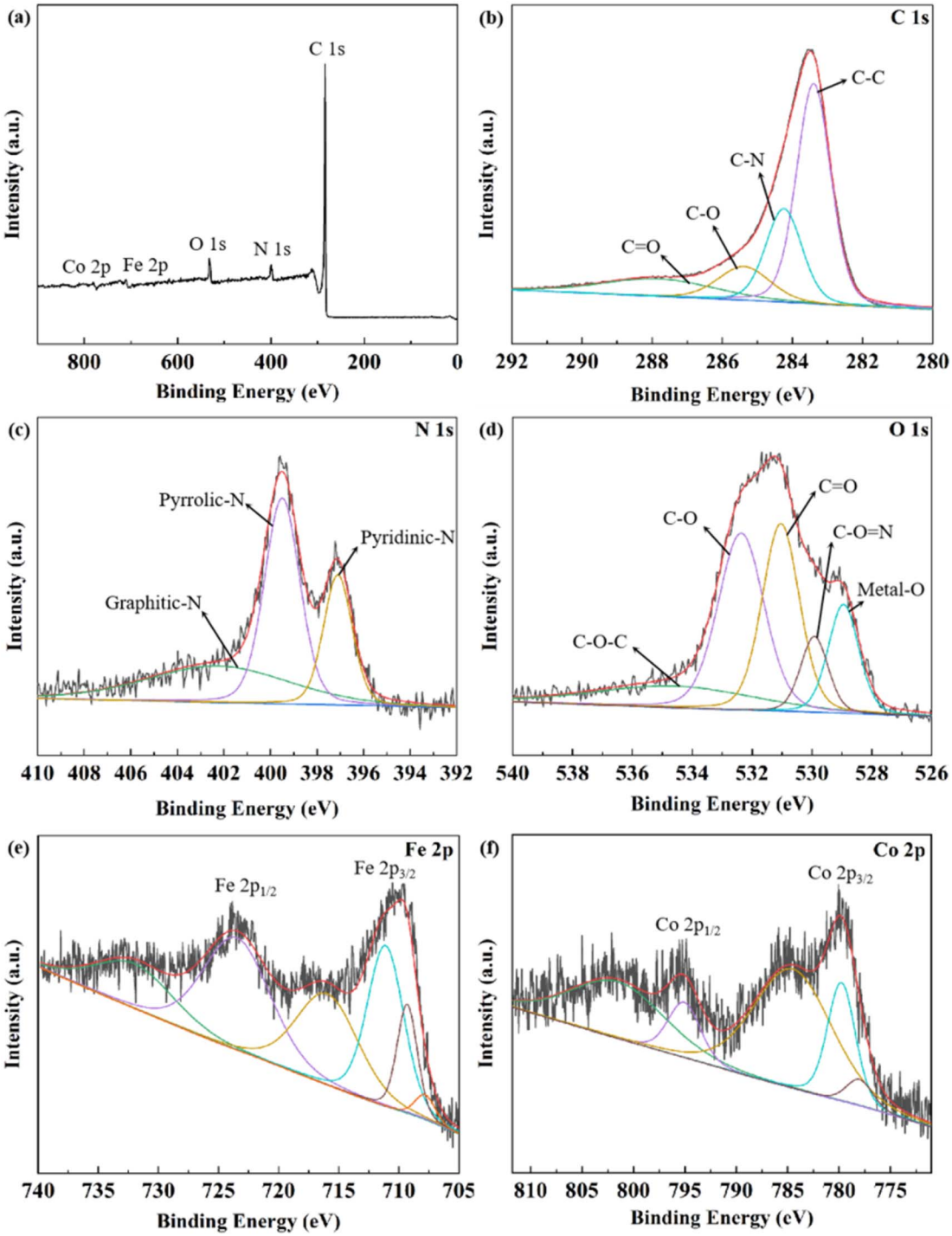

Fig. 5 XPS spectra of NCS/FeCo: (a) full; (b) C 1s; (c) N 1s; (d) O 1s; (e) Fe 2p, and (f) Co 2p spectra.

The ratio of D-band to G-band (I_D/I_G) is calculated to characterize the material's graphitization degree. Generally, the higher the I_D/I_G ratio, the lower the material's graphitization degree, indicating more defects and a higher degree of disorder. As shown in Fig. 6, the corresponding I_D/I_G for NCS/FeCo is 0.96. The loading of FeCo magnetic particles effectively improves the surface roughness of NCS microspheres and endows the surface of microspheres with a higher degree of defects. A higher defect degree is vital for controlling the dielectric properties of materials. In the electromagnetic environment, several material defects are employed as the polarization center, effectively enhancing the material's EWA ability.

3.5 VSM analysis

The vibrating sample magnetometer characterizes the NCS/FeCo's magnetic features. Fig. 7 displays the NCS/FeCo's

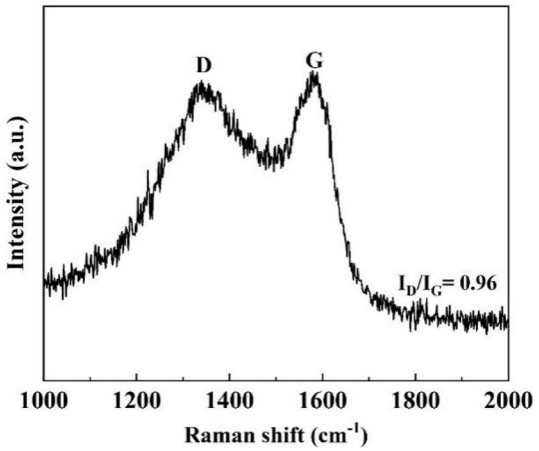

Fig. 6 Raman spectra of NCS/FeCo.

hysteresis loop at room temperature under an magnetic field of ±30 kOe. As presented in Fig. 7(a), the hysteresis loop of NCS/FeCo exhibits characteristics of ferromagnetic materials. The material's saturation magnetization (ms) reaches 17 emu g^{-1},[25] which is caused by the successful loading of magnetic metal particles. Fig. 7(b) presents a partial enlarged view of the part marked in red, highlighting the coercivity (H_C) of the material. Numerous studies have demonstrated that the coercivity significantly influences the composite's microwave absorbing features, and the H_C value of NCS/FeCo is 56 Oe, which is consistent with the coercivity characteristics of soft magnetic materials. The material's coercivity depends on the magneto-crystalline anisotropy introduced by FeCo particles.

3.6 Microwave absorbing performance and mechanism analysis

The VNA-based coaxial approach was employed to acquire the MAM's complex permittivity and permeability. Based on the transmission line theory, the microwave absorbing loss of the material in the 2–18 GHz frequency interval was computed through the subsequent formula (eqn (1)):

$$\mathrm{RL} = 20\log\left|\frac{Z_{in} - Z_0}{Z_{in} + Z_0}\right| \quad (1)$$

In the formula, Z_{in} and Z_0 describe the input and free space impedances (376.7 Ω) of the absorbing material, respectively, which is further expressed by the following formula (eqn (2)):

$$Z_{in} = Z_0(\mu_r/\varepsilon_r)^{1/2}\tanh[j(2\pi fd/c)(\mu_r\varepsilon_r)^{1/2}] \quad (2)$$

In eqn (2), the variables f, d, and c indicate the electromagnetic wave frequency, material thickness, and the light velocity (3×10^8 km s^{-1}), respectively. ε_r and μ_r denote the material's relative permittivity and permeability, respectively. At a certain frequency, the RL < −10 dB is generally considered the threshold for effective electromagnetic wave absorption. This value suggests that the absorption rate of the material to incident microwave radiation exceeds 90%.

Fig. 8 displays the NCS/FeCo composites' electromagnetic wave absorption capacity with different thicknesses in the 2–18 GHz band. At a 2.5 mm matching thickness, NCS/FeCo exhibits the maximum RL of −55.3 dB at 13.4 GHz, with the corresponding EAB of 11.28 GHz (6.72–18 GHz). At a thickness of just 2 mm, the maximum RL of NCS/FeCo is −48.5 dB, with the corresponding EAB of 9.12 GHz (6.56–15.68 GHz). The aforementioned results demonstrate that NCS/FeCo composites exhibit strong electromagnetic wave absorption across a wider frequency band under a thinner thickness, indicating good EWA efficiency.

It is noteworthy that when growing the matching thickness, the composite's maximum reflection loss exhibits a regular low-frequency shift, which is inseparable from the quarter wavelength resonance (eqn (3)):

$$t_m = \frac{n\lambda}{4} = \frac{nc}{4f_m\sqrt{\varepsilon_r\mu_r}}(n = 1,\ 3,\ 5\ldots) \quad (3)$$

In eqn (3), t_m denotes the composite's matching thickness, λ represents the electromagnetic wavelength, and f_m describes the matching frequency. As the material thickness is an odd multiple of the quarter wavelength, a half period phase deviation can be observed between the incident and reflected electromagnetic waves, and the amplitudes of the two waves cancel each other. Thus, this study further confirms that, in addition to dielectric and magnetic losses, interference loss is a significant aspect of electromagnetic wave reduction.

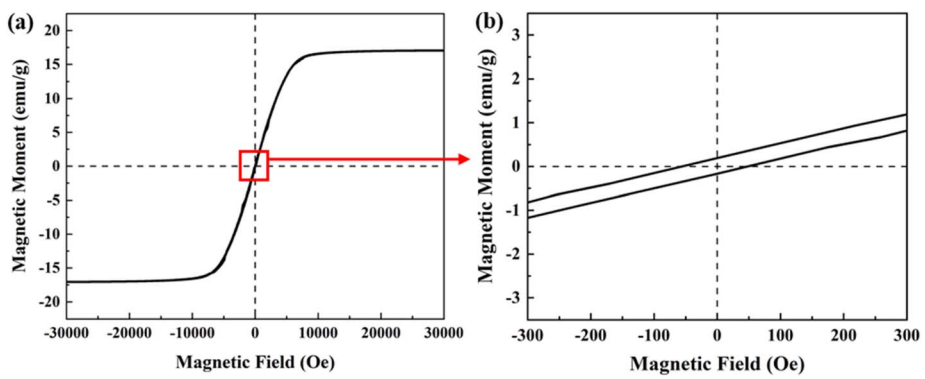

Fig. 7 Hysteresis loop for NCS/FeCo: (a) full curves; (b) partial enlarged image.

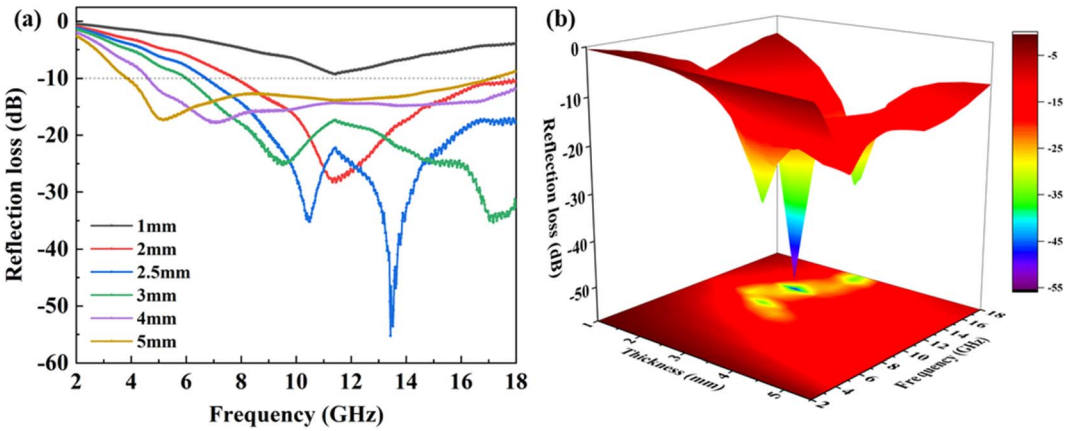

Fig. 8 Reflection loss plot for NCS/FeCo: (a) two-dimensional diagrams; (b) three-dimensional diagrams.

Furthermore, the NCS/FeCo composites' electromagnetic parameters were analyzed to explore their corresponding microwave absorbing features.

Fig. 9(a) depicts the complex permittivity (ε', ε'') and permeability (μ', μ'') curves of NCS/FeCo within the interval of 2–18 GHz. The composite's ε' value gradually decreases (2.0–5.4) as the frequency increases, demonstrating a standard carbon source dispersion phenomenon; the corresponding ε'' value initially increases and then decreases with the frequency (0.05–0.93). Meanwhile, the μ' value of the material fluctuates between 0.6 and 1.2, which is relatively stable. The μ'' value of the composite initially grows and then declines with frequency due to the successful loading of FeCo magnetic particles. It fluctuates with the frequency in the interval of 0.6–2.1, increasing from 0.6 to 2.1 in the 2–11.4 GHz band, and then declining from 2.1 to 0.6 within the interval of 11.4–18 GHz.

Several broad resonance peaks can be presented in the μ'' curve of the NCS/FeCo composite, revealing the material's polarization relaxation phenomenon in an alternating electromagnetic field. Based on existing research data, the materials' dielectric loss features are primarily determined based on their polarization behavior. Specifically, the polarization loss in the GHz band mainly involves dipole and interface polarizations. Notably, the high FeCo alloy loading and the rough surface structure of NCS microspheres in this system introduce numerous defects and heterogeneous interfaces. The mentioned deficiencies and heterogeneous interfaces considerably improve the materials' interfacial polarization effect. Additionally, the uniform distribution of FeCo alloy on NCS microspheres introduces more dipole polarization centers into the material within the high-temperature calcination process, effectively improving the dipole polarization relaxation of the material. Furthermore, due to the different electronegativities of CO and Fe, the binding state between them and NCS microspheres varies, resulting in uneven space charge distribution. This uneven space charge

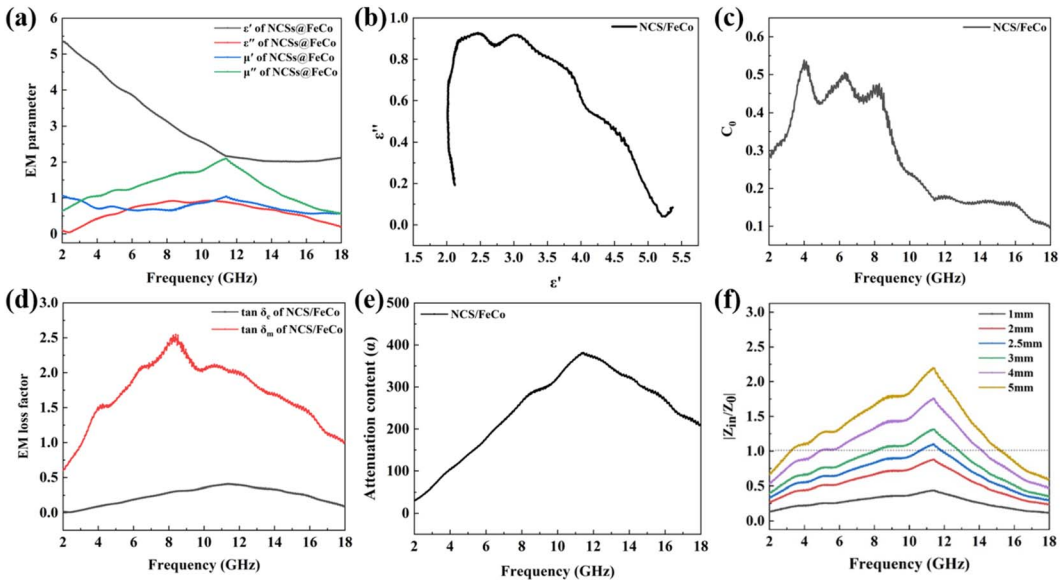

Fig. 9 The real and imaginary parts of the NCS/FeCo's complex permittivity and permeability at 2–18 GHz (a); Cole–Cole curve of NCS/FeCo (b); (c) C_0 value; (d) the tan δ_e and tan δ_m curves; (e) α value and (f) $|Z_{in}/Z_0|$ values.

distribution promotes electron transfer between materials and subsequent interface polarization.

The polarization relaxation process is further analyzed using the material's Cole–Cole curve, depicting a complex trajectory derived from the Debye equation (eqn (4)):

$$\left(\varepsilon' - \frac{\varepsilon_s + \varepsilon_\infty}{2}\right)^2 + \left(\varepsilon''\right)^2 = \left(\frac{\varepsilon_s - \varepsilon_\infty}{2}\right)^2 \quad (4)$$

Here, ε_s and ε_∞ depict the static and high-frequency dielectric constants, respectively.

Fig. 9(b) displays the NCS/FeCo microwave-absorbing composite's Cole–Cole curve. The semicircle appearing on the curve serves as the Cole–Cole semicircle, indicating the material's Debye relaxation procedure. Several Cole–Cole semicircles appear on the image of the sample, indicating that the material undergoes multiple Debye relaxation procedures. Additionally, the existence of several straight lines in the image reveals that conduction loss is also involved in the materials' dielectric loss mechanism.

Generally, the magnetic loss primarily involves hysteresis loss and eddy current loss (ECL), and domain wall, natural, and exchange resonances. As this experiment concentrates on the absorbing material's magnetic loss efficiency in the 2–18 GHz band, the domain wall resonance occurring just in the interval of 1–100 MHz is ignored. Moreover, since the hysteresis loss is insignificant in the weak magnetic field environment, the type of magnetic loss should focus only on natural and exchange resonances, and ECL. The subsequent equation determines the above loss types (eqn (5)):

$$C_0 = \mu''(\mu')^{-2} f^{-1} = 2\pi\mu_0\sigma d^2/3 \quad (5)$$

In eqn (5), C_0 is a constant independent of f, μ_0 indicates the vacuum permeability, and δ describes the conductivity. If the material's magnetic loss is entirely induced by the ECL, the value of C_0 will be kept unchanged regardless of the frequency variations. Fig. 9(c) displays the C_0 curve. The calculated C_0 value curve of the material exhibits significant fluctuation in the medium- and low-frequency band (<12 GHz), demonstrating the significant role of the resonance loss in this band. However, the C_0 value curve is relatively stable in the high-frequency interval (>12 GHz), revealing the strong influence of the ECL.

According to the above analysis of complex permittivity and permeability, the loss tangent (eqn (6) and (7)) of the material can be obtained through the subsequent relations:

$$\tan\delta_e = \varepsilon''/\varepsilon' \quad (6)$$

$$\tan\delta_m = \mu''/\mu' \quad (7)$$

The magnetic loss tangent ($\tan\delta_m$) is significantly larger than the dielectric loss tangent ($\tan\delta_e$) in the full range of 2–18 GHz, which reveals that the NCS/FeCo composite is an EWA material with magnetic loss as the main type.

The microwave-absorbing materials' comprehensive microwave-absorbing performance is often evaluated using the attenuation constant, as defined by (eqn (8)):

$$\alpha = \frac{\sqrt{2}\pi f}{c}\sqrt{\left(\mu''\varepsilon'' - \mu'\varepsilon'\right) + \sqrt{\left(\mu''\varepsilon'' - \mu'\varepsilon'\right)^2 + \left(\mu'\varepsilon'' + \mu''\varepsilon'\right)}} \quad (8)$$

The higher the calculated α, the better the absorbing material's comprehensive absorbing capacity. Fig. 9(d) displays the calculation results. As depicted in the image, the α value initially grows and then declines with the increase in frequency, reaching the peak value of 381.6 at 11.43 GHz, which aligns with the calculation result of reflection loss.

Furthermore, the IM ability plays a decisive role in the material's final absorbing ability. Fig. 9(e) displays the impedance matching curve of NCS/FeCo in the 2–18 GHz band. Notably, at a 2.5 mm thickness and a 10–13 GHz frequency range, the calculated Z value is very close to 1, which aligns with the result of reflection loss. This is primarily caused by the significant number of FeCo alloys that are loaded on the surface of NCS microspheres, which enhances the material's complex permeability and optimizes impedance matching. To achieve effective electromagnetic wave absorption, proper impedance matching should be ensured, allowing the electromagnetic waves to arrive into the material's interior and undergo scattering and multiple reflections.

Notably, N-doping makes an indispensable and crucial contribution to enhancing the electromagnetic wave absorption performance of this composite, and this effect is fully supported by the detailed XPS characterization data. In the PDA-derived carbon matrix, pyridine-N (binding energy: 402.43 eV), pyrrole-N (binding energy: 399.48 eV), and metal–O bonds (binding energy: 528.93 eV) are clearly detected. Both pyridine-N and pyrrole-N contain lone pairs of electrons that are not involved in bonding in their molecular structures; these lone pairs can form stable coordination bonds with free Fe^{2+}/Co^{2+} ions in the solution, constructing directional binding sites of "N-metal ions". During the subsequent calcination process at 750 °C under a nitrogen atmosphere, these coordination bonds not only effectively inhibit the deterioration of magnetic properties caused by the high-temperature agglomeration of FeCo particles but also guide FeCo particles to nucleate directionally on the surface of the carbon matrix with uniform sizes, laying a microstructural foundation for the subsequent synergistic matching of dielectric loss and magnetic loss.

At the same time, the presence of graphitic-N (binding energy: 397.08 eV) in the XPS results further enriches the functional dimensions of N-doping: graphitic-N exhibits high electrical conductivity, and its atomically dispersed characteristics can provide a large number of active sites for defect polarization inside the material. Under the action of an alternating electromagnetic field, these active sites become core centers for dipole polarization, significantly enhancing the polarization effect at the heterogeneous interface between the carbon matrix and FeCo particles. This interfacial polarization effect synergizes with the high defect concentration reflected by the I_D/I_G ratio of 0.96 in Raman analysis, jointly promoting the improvement of the material's dielectric loss capacity. Ultimately, it complements the magnetic loss of FeCo, optimizing

Table 1 EM absorption properties of FeCo/carbon absorbers

Materials	RL_{min} (dB)	EAB (GHz)	Thickness (mm)	Content (wt%)	Ref.
$Fe_{40}Co_{60}$@C	−36.4	Almost 5	3.0	50	26
FeCo/C@WC-2	−47.6	8.9	1.5	85	13
FeCo/C fiber	−59.9	5.1	2.5	Nondisclosure	27
TSH-Fe_3O_4/FeCo/C	−37.4	5.9	2.2	50	11
FeCo@C	−48.5	4.5	2.5	32	28
FeCo@CCA-100	−49.5	10.9	4.0	20	29
NCS/FeCo	−55.3	11.3	2.5	20	This work

the overall electromagnetic wave dissipation efficiency of the material.

In summary, the NCS/FeCo composites' electromagnetic wave absorption mechanism is summarized as follows: first, the load of FeCo alloy increases the material's magnetic loss ability, mainly through natural and exchange resonances, and ECL. Second, the FeCo alloy facilitates electron transfer between the FeCo alloy and the carbon material, resulting in stronger polarization relaxation at the heterogeneous interface. Simultaneously, the oxygen-including functional groups on the surface of NCS microspheres and the doped N atoms function as polarization centers, resulting in stronger dipole polarization relaxation. Third, the synergy of dielectric and magnetic losses consumes both electric and magnetic energies, thus enhancing the absorption of electromagnetic waves. Fourth, NCS/FeCo exhibits good IM features, allowing more electromagnetic waves to arrive into the material and be fully consumed, thereby enhancing absorption over a wider frequency band.

We compared the electromagnetic wave absorption performance of the NCS/FeCo composite material prepared in this study with other similar FeCo/C composite materials in recent years, and thus drew the following table (see Table 1). Obviously, NCS/FeCo composite materials have the most excellent and balanced electromagnetic wave absorption performance.

4 Conclusion

The current work presents the synthesis of polydopamine microspheres based on a self-polymerization reaction using dopamine monomer as raw material. Due to the high surface activity of dopamine, Co^{2+} and Fe^{3+} were adsorbed. Subsequently, nitrogen-doped carbon microspheres/FeCo alloy composite microwave-absorbing material (NCS/FeCo) was synthesized *via in situ* reduction using a high-temperature calcination method. Furthermore, its morphology distribution, chemical composition, disorder degree, and magnetic and electromagnetic factors were analyzed. At a 2.5 mm thickness, the maximum RL reaches −55.3 dB at 13.4 GHz, with the corresponding EAB of 11.28 GHz (6.72–18 GHz), indicating remarkable microwave absorbing performance. This is caused by the composite framework of carbon microspheres and the FeCo alloy, which forms more carbon magnetic heterogeneous interfaces and enhances impedance matching. Additionally, NCS/FeCo facilitates enhanced polarization relaxation, along with dielectric and magnetic loss mechanisms, establishing it as a high-efficiency microwave absorbing material. Meanwhile, the adsorption of metal ions by PDA is driven by the synergistic effect of strong covalent bonds and non-covalent bonds, resulting in high binding strength. After high-temperature calcination, the composite firmness between the two phases is further enhanced. Therefore, the composite structure constructed in this study has almost no potential risk of cobalt (Co) leaching. In future research, we will also attempt to replace cobalt with other metals such as nickel to further mitigate the risk of environmental exposure.

Conflicts of interest

There are no conflicts of interest to declare.

Data availability

Data will be made available on request.

Acknowledgements

This study was financially supported by the Jiangsu Province's 6th “333 Talents” 2022 Training Support Funding: Controllable Preparation of Carbon Doped N/Fe_3O_4 Coatings on the Surface of Carbon Fibers and Its Mechanism of Wave Impedance Influence. The authors would like to acknowledge the support of the CETC AV3672C vector network analyzer provided by Nantong University.

References

1 Z. J. Li, H. Lin, S. Q. Ding, *et al.*, Synthesis and enhanced electromagnetic wave absorption performances of Fe_3O_4@C decorated walnut shell-derived porous carbon, *Carbon*, 2020, **167**, 148–159.
2 M. Katiyar, *et al.*, Development of Low Density, Heat Resistant and Broadband Microwave Absorbing Materials (MAMs) for Stealth Applications, *Silicon*, 2018, **10**(5), 1831–1839.
3 D. Ding, Y. Wang, X. D. Li, *et al.*, Rational design of core-shell Co@C microspheres for high-performance microwave absorption, *Carbon*, 2017, **111**, 722–732.
4 M. T. Qiao, X. F. Lei, Y. Ma, *et al.*, Application of yolk-shell Fe_3O_4@N-doped carbon nanochains as highly effective

microwave-absorption material, *Nano Res.*, 2018, **11**(3), 1500–1519.

5 Z. H. Liu, *et al.*, Preparation and microwave absorbing property of carbon fiber/polyurethane radar absorbing coating, *RSC Adv.*, 2017, **7**(73), 46060–46068.

6 Y. Wei, *et al.*, Fabrication of TiN/Carbon nanofibers by electrospinning and their electromagnetic wave absorption properties, *J. Alloys Compd.*, 2018, **735**, 1488–1493.

7 C. Liu, J. Qiao, X. Zhang, *et al.*, Bimetallic MOF-derived porous CoNi/C nanocomposites with ultra-wide band microwave absorption properties, *New J. Chem.*, 2019, **43**(42), 16546–16554.

8 J. W. Ge, S. M. Liu, L. Liu, *et al.*, Optimizing the electromagnetic wave absorption performance of designed hollow $CoFe_2O_4$/CoFe@C microspheres, *J. Mater. Sci. Technol.*, 2021, **81**, 190–202.

9 S. P. Li, Y. Huang, D. Ling, *et al.*, Enhanced microwave-absorption with carbon-encapsulated Fe-Co particles on reduced graphene oxide nanosheets with nanoscale-holes in the basal plane, *J. Colloid Interface Sci.*, 2019, **544**, 188–197.

10 S. P. Li, Y. Huang, X. Ding, *et al.*, Synthesis of core-shell FeCo@S_iO_2 particles coated with the reduced graphene oxide as an efficient broadband electromagnetic wave absorber, *J. Mater. Sci. Mater. Electron.*, 2017, **28**(21), 15782–15789.

11 Y. Bao, R. Y. Guo, C. Liu, *et al.*, Design of magnetic triple-shell hollow structural Fe_3O_4/FeCo/C composite microspheres with broad bandwidth and excellent electromagnetic wave absorption performance, *Ceram. Int.*, 2020, **46**(15), 23932–23940.

12 B. Wen, H. B. Yang, Y. Lin, *et al.*, Synthesis of core-shell Co@S-doped carbon@ mesoporous N-doped carbon nanosheets with a hierarchically porous structure for strong electromagnetic wave absorption, *J. Mater. Chem. A*, 2021, **9**(6), 3567–3575.

13 Y. Xiong, L. L. Xu, C. X. Yang, *et al.*, Implanting FeCo/C nanocages with tunable electromagnetic parameters in anisotropic wood carbon aerogels for efficient microwave absorption, *J. Mater. Chem. A*, 2020, **8**(36), 18863–18871.

14 B. Huang, J. L. Yue, Y. S. Wei, *et al.*, Enhanced microwave absorption properties of carbon nanofibers functionalized by FeCo coatings, *Appl. Surf. Sci.*, 2019, **483**, 98–105.

15 X. Sun, J. Z. He, Z. M. Song, *et al.*, Sodiumphosphinate-assisted synthesis of P-doped FeCo microcubes and their electromagnetic scattering characteristics, *J. Alloys Compd.*, 2020, **820**, 8.

16 B. Yang, Y. Wu, X. P. Li, *et al.*, Surface-oxidized FeCo/carbon nanotubes nanorods for lightweight and efficient microwave absorbers, *Mater. Des.*, 2017, **136**, 13–22.

17 J. Zhao, C. L. Li and R. Liu, Enhanced oxygen reduction of multi-Fe_3O_4@carbon core-shell electrocatalysts through a nanoparticle/polymer co-assembly strategy, *Nanoscale*, 2018, **10**(13), 5882–5887.

18 H. H. Liu, Y. J. Li, M. W. Yuan, *et al.*, In situ preparation of cobalt nanoparticles decorated in N-doped carbon nanofibers as excellent electromagnetic wave absorbers, *ACS Appl. Mater. Interfaces*, 2018, **10**(26), 22591–22601.

19 J. Yang, J. Y. Li, J. Q. Qiao, *et al.*, Magnetic solid phase extraction of brominated flame retardants and pentachlorophenol from environmental waters with carbon doped Fe_3O_4 nanoparticles, *Appl. Surf. Sci.*, 2014, **321**, 126–135.

20 E. Prathibha, R. Rangasamy, A. Sridhar, *et al.*, Synthesis and characterization of Fe_3O_4/carbon dot supported MnO_2 nanoparticles for the controlled oxidation of benzyl alcohols, *ChemistrySelect*, 2020, **5**(3), 988–993.

21 Y. J. Wang, Y. Sun, Y. Zong, *et al.*, Carbon nanofibers supported by FeCo nanocrystals as difunctional magnetic/dielectric composites with broadband microwave absorption performance, *J. Alloys Compd.*, 2020, **824**, 9.

22 J. B. Chen, J. Zheng, F. Wang, *et al.*, Carbon fibers embedded with Fe^{III}-MOF-5-derived composites for enhanced microwave absorption, *Carbon*, 2021, **174**, 509–517.

23 M. Chen, L. L. Shao, J. J. Li, *et al.*, One-step hydrothermal synthesis of hydrophilic Fe_3O_4/carbon composites and their application in removing toxic chemicals, *RSC Adv.*, 2016, **6**(42), 35228–35238.

24 C. H. Zhou, C. Wu and M. Yan, Hierarchical FeCo@MoS_2 Nanoflowers with Strong Electromagnetic Wave Absorption and Broad Bandwidth, *ACS Appl. Nano Mater.*, 2018, **1**(9), 5179–5187.

25 X. Li, C. Huang, Z. L. Wang, *et al.*, Enhanced electromagnetic wave absorption of layered FeCo@carbon nanocomposites with a low filler loading, *J. Alloys Compd.*, 2021, **879**, 9.

26 Q. L. Tan, T. Li, U. R. Sajjad, *et al.*, Improved microwave absorbing properties of core-shell FeCo@C nanoparticles, *Mater. Res. Express*, 2019, **6**(7), 075034.

27 Y. Wang, C. H. Ye, N. Meng, *et al.*, FeCo Nanoparticles Embedded in Carbon Microfibers Derived from Conjugated Microporous Polymers for Enhanced Electromagnetic Wave Absorption, *ACS Appl. Nano Mater.*, 2025, **8**(20), 10623–10632.

28 L. Hu, H. Pan, L. H. Xu, *et al.*, A tunable structure lignin-derived carbon-based magnetic composite for efficient electromagnetic wave absorption, *Mater. Sci. Eng., B*, 2024, **302**, 117229.

29 Y. Guo, D. D. Wang, Y. Tian, *et al.*, FeCo alloy nanoparticle decorated cellulose based carbon aerogel as a low-cost and efficient electromagnetic microwave absorber, *J. Mater. Chem. C*, 2021, **10**(1), 126–134.